Numerical investigation of secondary flows in a constant-width wind-tunnel contraction

M. Bouriga, R. Taher and F. Morency
J. Weiss
julien.weiss@etsmtl.ca

Laboratoire TFT, École de technologie supérieure
Montréal
Canada

ABSTRACT

The flow inside a constant-width wind-tunnel contraction is simulated by solving the Reynolds-Averaged Navier-Stokes equations with an eddy-viscosity turbulence model. The results show the presence of longitudinal vortices near the sidewalls centreline. This confirms a former hypothesis involving the generation of skew-induced longitudinal vorticity within the sidewalls boundary layers. Detailed analysis reveals that the flow structure is influenced by viscous effects in the boundary layers and streamline curvature in the potential flow. Three-dimensional boundary-layer profiles on the contraction sidewall are analysed in the framework of the streamline co-ordinate system and its associated hodographic diagram. The resulting profiles help understand the generation of secondary flows and the associated longitudinal vorticity.

NOMENCLATURE

A_C	contraction ratio
c_f	skin-friction coefficient
d_{in}	Preston tube internal diameter
d_{ext}	Preston tube external diameter
H_1	contraction inlet height
H_2	contraction exit height
I_{inlet}	turbulence intensity at the inlet
$I_{t.s.}$	turbulence intensity in the test section
k	turbulent kinetic energy
L	contraction length (without extension)
l_{inlet}	turbulent mixing length at the inlet
L_C	total contraction length
n	apparent order of the numerical method
p	static pressure
r	grid refining ratio
U_{exit}	flow velocity at the contraction exit
U_{ref}	reference velocity
U_e^*	local transformed streamwise velocity
(U^*,V^*,W^*)	transformed velocity field in the streamline co-ordinate system
w	contraction width
x	longitudinal position in the contraction
x_m	location of the match point in the contraction
y	vertical position in the contraction
y^+	dimensionless wall distance of the first cell normal to wall
z	spanwise position in the contraction
δ	boundary layer thickness
v	kinematic viscosity
ω	specific dissipation rate
(ξ,η,ζ)	streamline co-ordinate system

Acronyms

CFD	Computational Fluid Dynamics
GCI	Grid Convergence Index
NPL	National Physical Laboratory
RANS	Reynolds-Averaged Navier-Stokes
SIMPLE	Semi-Implicit Method for Pressure-Linked Equations
TFT	Thermo-Fluid for Transport Laboratory

1.0 INTRODUCTION

In a wind tunnel, the contraction plays a major role in achieving an optimal flow quality prior to entering the test section. Inside the contraction, the flow is not only being accelerated to reach the velocities needed in the working section, but its quality is also improved by the reduction of turbulence level and flow non-uniformity that may otherwise negatively affect the flow quality

in the test section. Axisymmetric contractions are considered the optimal choice when it comes to achieving a uniform flow with low turbulence levels. For manufacturing reasons, rectangular or octagonal designs are often used as well. Finally, 'two-dimensional', i.e. constant-width, contractions are often considered for low-speed, academic wind tunnels, mostly because of the simplicity of their construction and in spite of the limitation in contraction ratio compared to three-dimensional designs of the same height[10].

The design of a wind-tunnel contraction should take contradicting constraints into account. For instance, a long contraction is preferred when it comes to reducing the risk of flow separation. However, cost and space considerations frequently make designing a long contraction impractical. In addition, reducing the contraction length helps minimise the boundary-layer thickness at the entrance of the test section, which increases the useful test area[4]. Therefore, there is an optimum shape and length that ensures a fair flow quality while excluding any risk of separation. Contraction design has been an extensive research topic. Most design methods are based on the solution of a potential flow problem coupled with either analytic boundary-layer separation criteria or numerical solutions of the boundary-layer equations. Perhaps the most well-known design methods are those of Morel[25,26] and Bell and Metha[4].

The possible occurrence of secondary flows near the corners forming the intersection of the sidewalls in three-dimensional, rectangular contractions has been known for a long time[10]. This type of secondary flow, which is caused by the convergence of surface streamlines towards the contraction corners, are generally thought to be minimised in octagonal contractions, and nonexistent in two-dimensional designs[10]. Another type of secondary flow, which is specific to constant-width contractions, was suggested by Mokhtari and Bradshaw[29], and is believed to lead to the formation of longitudinal vortices close to the sidewall centreline. This is an example of skew-induced secondary flow according to the terminology of Bradshaw[8]. The possible occurrence of this phenomenon was backed by experimental measurements of skin-friction and velocity profiles in a constant-width contraction at Imperial College[29], and may explain the deformed velocity profiles observed on the test-section sidewalls of the National Physical Laboratory (NPL) 50in × 9in Boundary-Layer Wind Tunnel[9].

Recently, Mohammed-Taifour *et al*[23] reported that the measured boundary-layer thickness at the exit of the constant-width contraction of the Thermo-Fluid for Transport Laboratory's (TFT) Boundary-Layer Wind Tunnel was larger near the sidewalls centrelines than elsewhere in the contraction exit plane. A preliminary numerical analysis performed by Bouriga *et al*[6] revealed the presence of longitudinal vortices on the sidewalls, thus confirming Mokhtari and Bradshaw's[29] hypothesis. However, due to the preliminary nature of these results, no satisfactory comparison was made between the numerical results of Bouriga *et al*[6] and the experimental results of Mohammed-Taifour *et al*[23].

The purpose of the present article is to extend the results of Bouriga *et al*[6] by presenting a detailed numerical investigation of secondary-flow effects on the contraction sidewalls of the TFT Boundary-Layer Wind Tunnel. The simulation is performed by solving the Reynolds-Averaged Navier-Stokes (RANS) equations with an linear eddy-viscosity turbulence model. The goal is not only to provide a physical explanation of the experimental results of Mohammed-Taifour *et al*[23], but also to describe in details the structure of the flow in the contraction and to highlight possible differences between the qualitative flow structure and the conceptual model proposed by Mokhtari and Bradshaw[29]. This work is part of a growing trend of Computational Fluid Dynamics (CFD) investigations for wind-tunnel design and optimisation[11,24].

2.0 CONTRACTION GEOMETRY AND EXPERIMENTAL RESULTS

The TFT Boundary-Layer Wind Tunnel is described in details in Mohammed-Taifour *et al*[23]. Its constant-width contraction has an area ratio of $A_C = 9$ and a matched-cubic shape that was designed with a match point located at 70% of the contraction length[26]. Following the recommendations of Mehta and Bradshaw[20], an additional constant-height section of 0·2m in length was added to allow some reduction of flow non-uniformity before the entrance of the working section. The parameters of the contraction are summarised in Table 1.

Table 1
Design parameters of the contraction in the TFT boundary-layer wind tunnel

Parameter			Value
Contraction ratio	A_C	–	9
Length without extension	L	m	1·65
Total length	L_C	m	1·85
Inlet height	H_1	m	1·35
Exit height	H_2	m	0·15
Length to height ratio	L/H_1	–	1·22
Match point	x_m/L	–	0·7
Contraction width	w	m	0·6

The boundary-layer thickness near the exit of the contraction is presented in Fig. 1. It was measured using a Pitot probe at a reference velocity of $U_{ref} = 30\text{ms}^{-1}$, where U_{ref} is defined as the velocity at the centre of the contraction exit plane. The custom-built, square-ended Pitot probe had an internal diameter of 1·6mm and an external diameter of 2·4mm, which resulted in an uncertainty of about ±1mm in the boundary-layer thickness. Additional hot-wire measurements revealed that the turbulence intensity in the free-stream is about 0·05%[23]. Three definitions of the boundary-layer thickness are used in Fig. 1: δ_{95} (respectively δ_{99} and $\delta_{99.5}$) is the position where the local velocity equals 95% (respectively 99% and 99·5%) of the (uniform) velocity in the potential flow (note that by construction, $\delta_{95} < \delta_{99} < \delta_{995}$). An interesting feature of Fig. 1 is the small 'bulge' of the δ_{995} thickness close to the centre of each side wall: at this location, the velocity profiles appear to be deformed compared to profiles further away from the centreline. This anomaly, which is the first indication of possible longitudinal vortices near the sidewalls centreline, will be discussed in more details in Section 4.
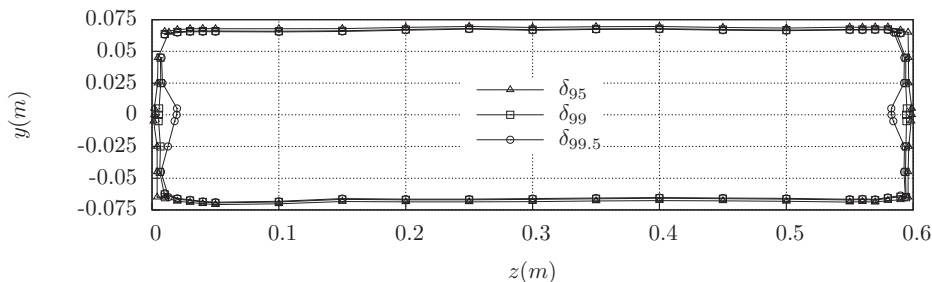

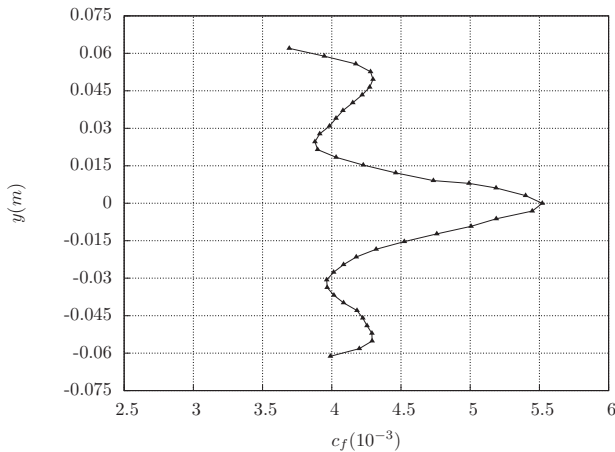Figure 1. Measured boundary-layer thickness at the contraction exit ($U_{ref} = 30\text{ms}^{-1}$).

Figure 2. Variation of the skin-friction coefficient along the contraction
sidewall, calculated using the Patel calibration (U_{ref} = 30ms^{-1}).

For velocities above U_{ref} = 30ms^{-1}, the boundary layer at the contraction exit is turbulent on all four walls[23]. This was verified by analysing the shape of the velocity profiles at several reference velocities ranging from 5ms^{-1} to 30ms^{-1} and confirmed by subsequent hot-wire measurements. At a reference velocity of U_{ref} = 30ms^{-1}, measurements with a stethoscope indicated that laminar-turbulent transition occurs between 0·30m and 0·45m upstream of the contraction exit plane.

The variation of the skin-friction coefficient c_f along the left sidewall near the contraction exit plane is presented in Fig. 2 for U_{ref} = 30ms^{-1}. It was measured by vertically traversing a Preston tube on the sidewall surface (z = 0m in Fig. 1). The custom-built Preston tube had an internal diameter of d_{in} = 0·45mm and an external diameter of d_{ext} = 0·71mm. The static pressure was measured at a pressure tap located 0·08m upstream of the contraction exit and the dynamic pressure was converted to shear stress using Patel's calibration law. The uncertainty in c_f resulting from this procedure is about ±3%[30]. The small asymmetry of c_f in Fig. 2 can be explained by imperfections in the contraction geometry caused by its manual construction[23].

The variation c_f clearly exhibits a peak near the sidewall centreline. This is in contrast with the measurements of Mokhtari & Bradshaw[29], who observed a dip in c_f at the exit plane of their 3:1 contraction and a small peak further downstream. Here also, further analysis of the data is deferred to Section 4.

3.0 NUMERICAL SETUP

3.1 Geometry and grid

Taking the contraction symmetries into account, the geometrical model is reduced to one quarter of the actual device (Fig. 3). In addition, the geometrical model contains a 0·15m extension after the actual contraction exit in order to reduce the effects of the outlet boundary condition on the results. The model boundaries consist of an inlet and exit, the curved upperwall, the sidewall and two symmetry planes. One test case was run without any symmetry plane in order to rule out any influence of those planes on the simulation results.
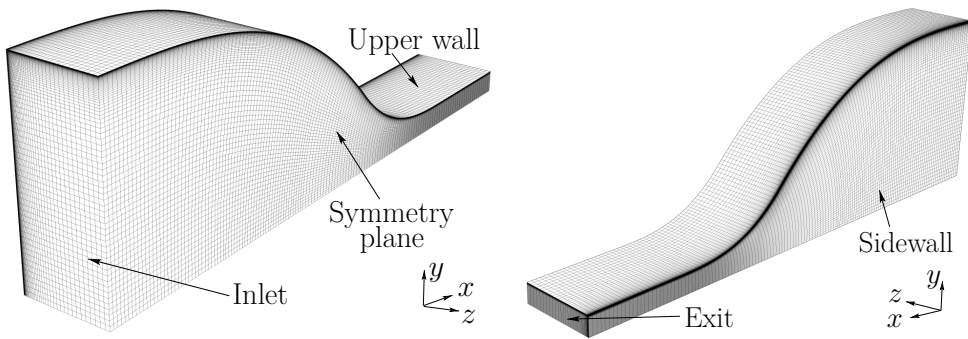
Figure 3. Computational grid of the wind-tunnel contraction (units in metres).

The fluid domain was discretised with a block-structured hexahedral mesh using the commercial grid generation software ICEM CFD. Discretisation was realised using an *H*-grid topology. Although the geometry is quite simple and does not contain sharp edges or complex features, care must be taken in order to ensure acceptable mesh quality. The domain was therefore divided in multiple blocks, whose edges were associated with curves orthogonal to the flow streamlines.

Since the flow details near the walls are the main objective of the study, a particular emphasis was made on the grid quality and density near the walls. The first node distance to the wall was set to ensure that $y^+ \leq 1$ anywhere in the domain, enabling the solver to capture the viscous sublayer.

To investigate the grid convergence behaviour, three different grids were generated. An initial coarse mesh was refined by a factor $1\cdot3 \times 1\cdot3 \times 1\cdot3$ to yield a medium size grid which was in turn refined with the same factors to produce the fine grid. Refining was performed by ICEM CFD which kept the first wall distance constant for all the grids. The overall grid size was $9\cdot51 \times 10^5$ cells for the initial coarse grid, $2\cdot10 \times 10^6$ cells for the medium grid and $4\cdot61 \times 10^6$ cells for the fine grid. The coarse grid is illustrated in Fig. 3.

3.2 Numerical models

The flow-field computations were performed by solving the three-dimensional, incompressible, steady-state, Reynolds-Averaged Navier-Stokes equations using the open-source finite-volume CFD toolbox OpenFOAM 2.1. A detailed presentation and discussion of the solver theory and implementation is provided by Jasak[18] and Weller *et al*[31]. The numerical calculations were performed using the OpenFOAM steady-state solver simpleFoam implementing the SIMPLE algorithm, first introduced by Patankar and Spalding[28], for the pressure-velocity coupling in the Navier-Stokes system.

Turbulence properties were computed using the SST $k-\omega$ model[16]. The model is derived from the original $k-\omega$ model[32] and a transformed version of the $k-\varepsilon$ model. The mixed behaviour inherited from both models enables the SST $k-\omega$ model to retain the advantages of both. The model simulates the viscous sublayer without the need of damping functions while having a similar behaviour to the $k-\varepsilon$ family models in free-stream regions. As any two-equation model, the SST $k-\omega$ model consists of two partial differential equations describing the transport of the turbulent kinetic energy k and a dissipation property, namely the specific dissipation rate ω in this case. For the case of an incompressible flow with $\rho = 1$, the transport equations of the model for both fields k and ω are as follows:

$$\frac{\partial k}{\partial t} + u_j \frac{\partial k}{\partial x_j} = \tau_{ij} \frac{\partial u_i}{\partial x_j} - \beta^* \omega k + \frac{\partial}{\partial x_j}\left[(\nu + \sigma_k \nu_t)\frac{\partial k}{\partial x_j}\right], \qquad \ldots (1)$$

$$\frac{\partial \omega}{\partial t} + u_j \frac{\partial \omega}{\partial x_j} = \frac{\gamma}{v_t} \tau_{ij} \frac{\partial u_i}{\partial x_j} - \beta \omega^2 + \frac{\partial}{\partial x_j}\left[(v + \sigma_\omega v_t)\frac{\partial \omega}{\partial x_j}\right] + 2(1-F_1)\sigma_{\omega2}\frac{1}{\omega}\frac{\partial k}{\partial x_j}\frac{\partial \omega}{\partial x_j}.$$

$$\ldots (2)$$

As in the case of other RANS models, turbulence effects are accounted for by the additional eddy viscosity v_t, which is computed from the values of k and ω using:

$$v_t = \frac{a_1 k}{\max(a_1\omega; \Omega F_2)},$$

$$\ldots (3)$$

where Ω is the absolute value of the vorticity, and where coefficients F_1 and F_2 are computed with the following relations:

$$F_1 = \text{Tanh}\left\{\min\left[\max\left(\frac{\sqrt{k}}{0\cdot09\omega y}; \frac{500v}{y^2\omega}\right); \frac{4\rho\sigma_{\omega2}k}{CD_{k\omega}y^2}\right]^4\right\},$$

$$\ldots (4)$$

$$F_2 = \text{Tanh}\left[\max\left(2\frac{\sqrt{k}}{0\cdot09\omega y}; \frac{500v}{y^2\omega}\right)^2\right],$$

$$\ldots (5)$$

$$CD_{k\omega} = \max\left(2\rho\sigma_{\omega2}\frac{1}{\omega}\frac{\partial k}{\partial x_j}\frac{\partial \omega}{\partial x_j}; 10^{-20}\right).$$

$$\ldots (6)$$

The closure coefficients of the model are:

$$\sigma_{k1} = 0\cdot85, \quad \sigma_{\omega1} = 0\cdot5, \quad \sigma_{\omega2} = 0\cdot856, \quad \beta_1 = 0\cdot075, \quad a_1 = 0\cdot31,$$

$$\beta^* = 0\cdot09, \quad \kappa = 0\cdot41, \quad \gamma_1 = \frac{\beta_1}{\beta^*} - \sigma_{\omega1}\frac{\kappa^2}{\sqrt{\beta^*}}.$$

The convection terms of the flow equations were discretised using the second-order upwind scheme. All other terms (diffusion terms and gradients) were discretised using the second-order linear (central) scheme. In the velocity equations, an enhanced version of the second-order upwind scheme, which accounts for the flow direction, was used.

The linear algebraic systems arising from the discretisation of the velocity and turbulence equations were solved with the preconditioned biconjugate gradient method (PBiCG) with a preconditioner based on the diagonal incomplete LU factorisation (DILU). The discretised pressure equation is solved with the algebraic multigrid method (AMG) with the lowest multi-grid level containing 20 cells. Solution convergence was checked by monitoring the evolution of the initial residual between the time steps. As with other decoupled methods, the SIMPLE algorithm uses equation under-relaxation to ensure stability of the solution process. In the present study, the pressure, velocity and turbulence equations were under-relaxed with factors of 0·3, 0·7 and, 0·5 respectively.

3.3 Boundary conditions

The computations involved solving the transport equation for the pressure, the velocity **U**, the turbulent kinetic energy k and the specific dissipation rate ω. The von Neumann boundary condition was set for the pressure ($\partial p/\partial n = 0$) at the contraction exit, whereas Dirichet boundary conditions were used for **U**, k and ω at the entrance. No-slip conditions for the velocity were imposed on the contraction walls and the normal gradients of the rest of the variables were set to zero.

The inlet velocity was defined by a profile approximating an incoming flow with an existing boundary layer. The inviscid zone was modeled with a constant velocity $U_{inlet} = 3\cdot3\text{ms}^{-1}$ in order to match the experimental value of $U_{ref} = 30\text{ms}^{-1}$ at the contraction exit. The boundary-layer zone was approximated with a parabolic profile extending from the no-slip wall to a thickness of 0·005m. This value was chosen since it approximates the thickness of the laminar boundary layer developing downstream of the last turbulence screen in the wind-tunnel's settling chamber[21]. The turbulence level at the entrance of the contraction was obtained from its measured value in the test section,[23] $I_{t,s} \cong 0\cdot05\%$ Assuming Batchelor's classical reduction factors for homogeneous turbulence in a converging nozzle[3], this corresponds to a turbulence level of about $I_{inlet} \approx 2\%$ at the contraction inlet. The specific dissipation rate ω was calculated from the mixing length l_{inlet}, which was estimated to be roughly equal to the wire diameter (0·7mm) of the last turbulence screen in the settling chamber[15]. Sensitivity studies performed with different values of I_{inlet} and ω at the contraction inlet showed that these parameters do not have a strong influence on the simulation results[5].

3.4 Modified turbulence model

At a reference velocity of $U_{ref} = 30\text{ms}^{-1}$, the boundary layer at the contraction exit is turbulent, which means that laminar-turbulent transition occurs on the contraction walls. In order to model the transition process, the common approach of dividing the fluid domain into a laminar and a turbulent zone was chosen. This approach is practical, since acoustic measurements on one of the sidewall's centreline showed that transition actually occurs between 0·45 and 0·30m upstream of the contraction outlet.
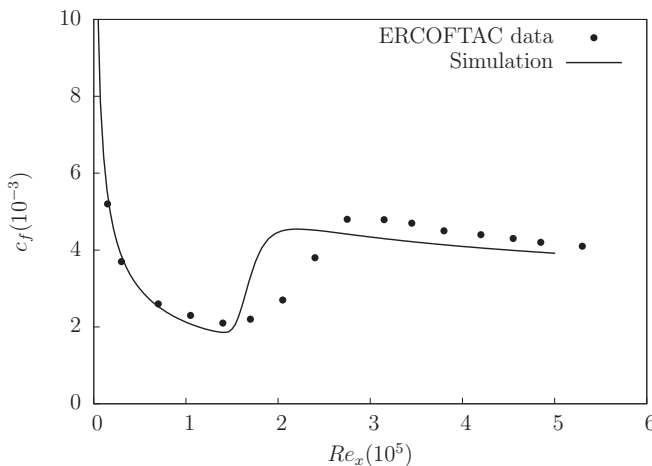

Figure 4. Calculated skin friction coefficient on a flat plate with transition, compared to experimental data from the ERCOFTAC T3A case.

Many CFD packages provide the possibility to set a given fluid zone as laminar. However, the standard turbulence models implemented in OpenFOAM do not offer such choice. The SST $k - \omega$ model in OpenFOAM was therefore adapted in order to allow specifying fully laminar regions in the computational domain. The basic idea is to set the eddy viscosity to zero in a fluid zone that the user considers to be laminar. This modification makes it possible to simulate a laminar-turbulent transition in OpenFOAM, although in very rudimentary manner.

The modified turbulence model was first applied to the case of the flow over a flat plate without pressure gradient. The test case was set up to represent the T3A validation case of the European Research Consortium on Flow, Turbulence and Combustion (ERCOFTAC)[14]. According to this experimental database, transition occurs at a Reynolds number $Re_x \cong 1\cdot4 \times 10^5$. Therefore, the transition location used in the modified model was set to $x = 0\cdot5$m downstream of the flat plate leading edge. Fig. 4 shows the computed skin friction c_f over the plate as a function of the Reynolds number, together with the ERCOFTAC T3A data. The discrepancy between the predicted distribution and the ERCOFTAC data is less than 15% downstream of the transition zone, which gives confidence in the use of the modified turbulence model.

For the flow-field simulations in the contraction, the transition plane was fixed at 0·45m upstream of the contraction exit. Further computations with the transition at 0·30m from the exit showed very little effects on the flow structure, except for a small variation in the value of the boundary-layer thickness at the contraction exit.

3.5 Run control

The simulations were run in parallel on a Dual Intel Westmere EP Xeon 5650 cluster with 3GB memory per processor core and an InfiniBand internodal network. The computations were run until the residuals of all transport equations were reduced by at least six orders of magnitude.

3.6 Grid convergence

Discretisation errors were estimated using the GCI method described in Celik *et al*[13]. Error estimation with the GCI method requires at least three successive refined grids. The grid disretisation error of the finest grid is estimated by calculating the fine-grid convergence index defined as:

$$GCI_{fine} = \frac{1\cdot25e_a^{21}}{r_{21}^n - 1}, \qquad \dots (7)$$

where $e_a^{21} = |(\phi_1 - \phi_2)/\phi_1|$ is the relative error of a selected global or local variable ϕ obtained from the first two grid levels, r_{21} is the refinement factor between the first and the second grid levels, and n is the apparent order of the numerical methods used in the computations.

In the present simulation, the selected variable ϕ used to estimate the error is the integral of the wall shear stress on the sidewall at the contraction exit, defined as:

$$\phi = \int_{y=0}^{y=0\cdot075} \tau_w(y)\mathrm{d}y. \qquad \dots (8)$$

As mentioned before, successive refined grids were obtained by refining each grid level with the same refinement factor $r = r_{21} = r_{32} = 1\cdot3$, which is the minimum recommended value to perform the GCI method[13].

The estimated apparent order of the numerical methods is roughly $n \approx 4$, meaning that the numerical methods are effectively at least second-order accurate. Meanwhile, the errors calculated
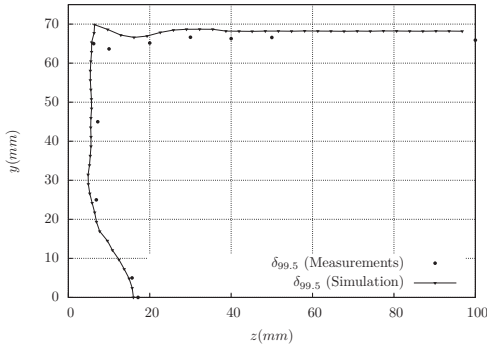
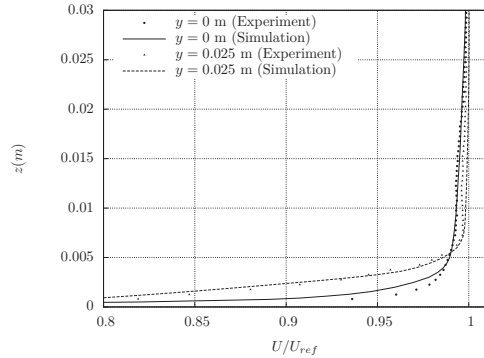Figure 5. Boundary-layer thickness δ_{995} obtained from experiments[23] and RANS simulations.

Figure 6. Measured and computed velocity profiles at the contraction exit at the locations y = 0m and y = 0·025m.

by the GCI method showed that the numerical uncertainty of the fine grid solution of ϕ is around $GCI_{fine} \approx 0\cdot25\%$ while the approximate relative errors remain below 0·4% for all grids.

3.7 Comparison with experimental data – validation

Results from the numerical simulation were extracted at the contraction exit (x = 1·85m), where the experiments were made, thus allowing a comparison between the experimental and numerical data.

Figure 5 shows a comparison between the velocity contours at the contraction exit obtained experimentally and numerically. Only the δ_{995} contour is represented since the other contours do not exhibit particular features. Qualitatively, the agreement is excellent since the observed increase in boundary-layer thickness is reproduced by the simulation. The simulated boundary layer is slightly thinner than in the experimental case. This is mainly due to the uncertainty in position and extent of the transition process. Indeed, calculations of the turbulent boundary-layer growth from the transition zone down to the contraction exit showed that moving the transition point in the computational domain by ±0·1m can result in a change of the boundary-layer thickness of at least ±1·5mm. On the other hand, this observed small quantitative difference of the boundary-layer thickness is not expected to be an issue for the analysis of the flow structure that will be done in Section 4.

Figure 6 shows normalised boundary-layer profiles obtained experimentally and numerically at two vertical positions on the sidewall at the contraction exit plane. y = 0m refers to a position on the sidewall centreline and y = 0·025m refers to a position slightly above the centreline. The difference in the shape of the profiles is a consequence of the longitudinal vortices that will be discussed in detail in the next section. It can be seen that the simulation accurately reproduces the difference in the profile shapes, although there is a slight discrepancy between the experimental and numerical results very near the wall.

Finally, Fig. 7 shows a comparison between the skin-friction distribution obtained experimentally and numerically. The calculated skin-friction distribution exhibits a peak near the centreline of the sidewall which is very similar to that observed experimentally. Nevertheless, the agreement between simulation and experiments is less good than in Fig. 5 and Fig. 6.

Based on the data shown in Figs 6 and 7, it appears that the discrepancies between experimental and numerical results are limited to the very near-wall region. The most likely explanation for these differences is the limitation of linear eddy-viscosity models to accurately reproduce several aspects of secondary-flow situations like streamline curvature and vortical motions[32]. Indeed, exploratory
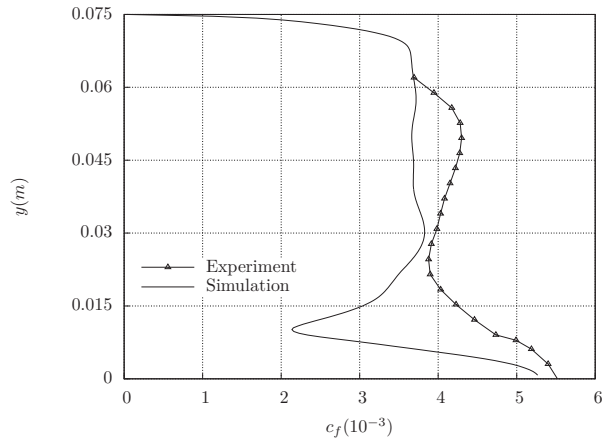
Figure 7. Comparison between measured and calculated skin-friction distributions at the contraction exit.
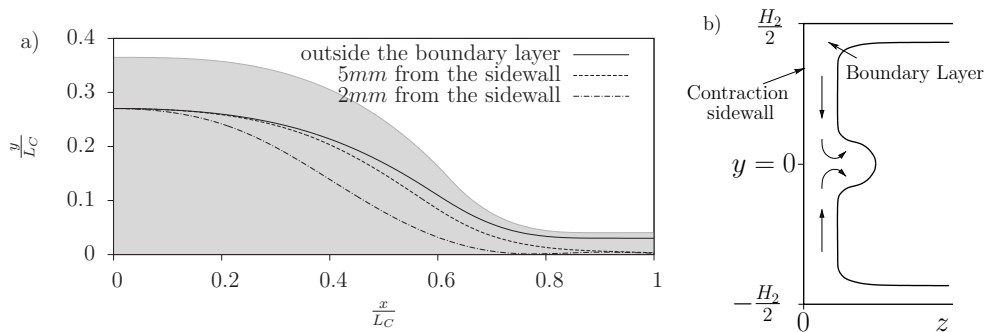

Figure 8(a). Effect of lateral pressure gradient on the streamline deflection outside and inside the sidewall boundary layer. (b) Sketch of associated vortex pattern at the contraction exit.

simulations with the Spalart-Allmaras and several variants of the $k - \varepsilon$ turbulence models have shown that the results are not very sensitive to the actual (eddy-viscosity) model chosen for the simulation[5]. Despite these limitations, and since the goal of the present simulation is to better understand the qualitative flow structure in the contraction, it is felt that the proposed approach of a RANS simulation with a linear eddy-viscosity turbulence model offers the best compromise between computing time, simplicity of data processing, and accuracy and usefulness of the results.

4.0 FLOW FIELD ANALYSIS

The hypothetical vortex pattern suggested by Mokhtari and Bradshaw[29] is best explained in terms of the confluence of near-wall streamlines towards the centreline of each contraction sidewall. Referring to the co-ordinate system introduced in Fig. 3, the lateral pressure gradient $\partial p / \partial y$ induced by the streamline curvature in the potential flow region deflects the near-wall streamlines more strongly, owing to their lower momentum. Because this effect occurs symmetrically on both sides of the contraction, the confluence of near-wall streamlines leads to a thickening of the boundary layer near the sidewall centreline, and to a pair of counter-rotating vortices aligned in the longitudinal direction. This phenomenon is illustrated in Fig. 8(a), which shows three computed streamlines
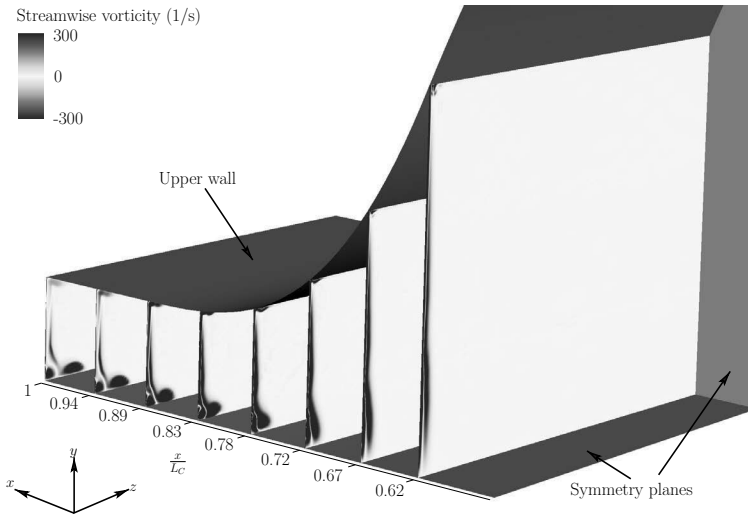
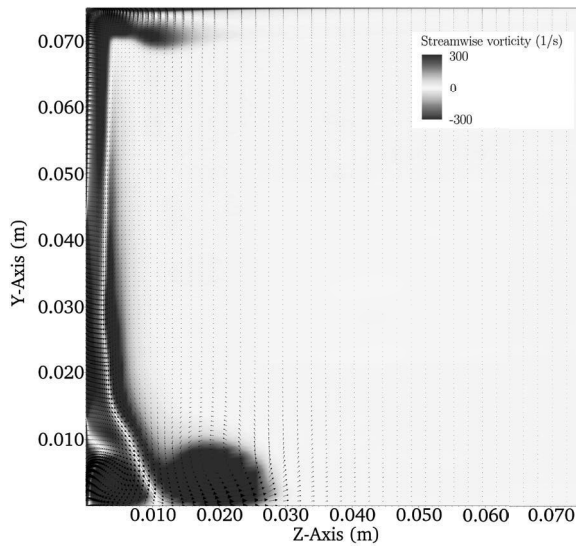Figure 9. *x*-vorticity contours in selected *y – z* planes.

Figure 10. Close-up of velocity field and longitudinal vorticity contours at $x/L_C = 0.89$.

originating at nearly two-third of the contraction half-height. It is clear that the streamlines originating near the sidewall are more deflected than the one originating in the potential flow. Furthermore, the streamline closest to the wall is also the most deflected, which is consistent with the conceptual model of a boundary layer deflected by a lateral pressure gradient. A sketch of the associated vortex pattern is presented in Fig. 8(b). For reference, the boundary-layer thickness at the contraction exit is $\delta \approx 6$mm away from the centreline.

This simple model of streamline confluence, which is based on inviscid secondary-flow considerations and could as well have been explained in terms of the skewing of vorticity vectors inside the sidewall boundary layer[2,12,8,17], should lead to a decrease of the friction coefficient c_f near the
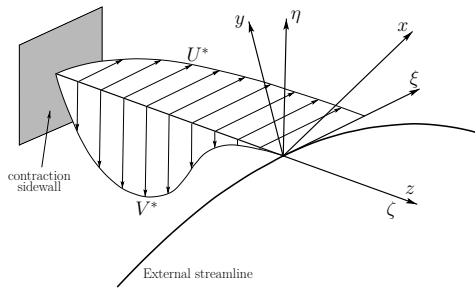
Figure 11. Typical three-dimensional boundary layer with its associated local streamline co-ordinate system.
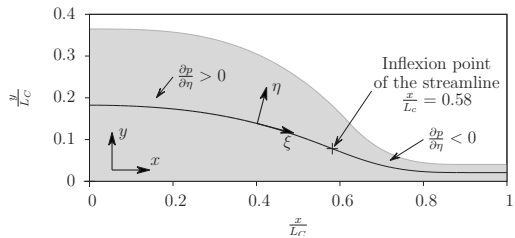

Figure 12. Selected streamline for velocity-profiles transformations.

sidewall centreline at the contraction exit. This decrease was indeed observed by Mokhtari and Bradshaw[29] in their constant-width contraction. On the other hand, this conceptual model is also oversimplifed since it doesn't take into account the cross-flow profile of the sidewall boundary layer. Indeed, Mokhtari and Bradshaw[29] themselves suggested that the small peak in c_f observed further downstream in the test section of their wind tunnel might be caused by a second pair of vortices, of opposite direction to the main ones, which would be linked to the cross-flow profile of the boundary layer in the wind-tunnel contraction.

To better illustrate the flow structure close to the contraction sidewall, Fig. 9 shows the longitudinal vorticity contours on cut planes at different locations inside the contraction. This figure reveals a flow of considerable complexity. Close examination of the $x/L_C = 0.89$ plane in Fig. 10 shows that two well-formed pairs of vortices are present at the contraction exit. On the computed half-height, a large, negative-circulation vortex extends up to 0.03m from the sidewall. Below, a smaller, positive-circulation vortex is observed within the first cm from the wall. Finally, a thin, near-wall region of negative vorticity can be seen under the secondary vortex. Because of symmetry, similar features of opposite direction would be observed on the other half-height of the contraction but are not represented in Figs 9 and 10.

The main, negative-circulation vortex in Figs 9 and 10 is consistent with the simple model of streamline confluence presented above. It is created by the downward motion of low-momentum fluid inside the sidewall boundary layer. Although the discrete vortex can't be recognised until far downstream in the contraction ($x/L_C \cong 0.78$), its formation begins much earlier. A significant downward motion can clearly be seen at $x/L_C = 0.62$. Further investigations showed that this downward motion is initiated after a very short distance downstream of the contraction inlet, although it remains weak and hard to discern from the general flow features. At the contraction exit, the main vortex deflects the fluid towards the potential flow region, which in turns increases the boundary-layer thickness near the sidewall centreline, as observed in Figs 1 and 5. Although the main vortex appears very large in Fig. 9, its influence on the boundary-layer thickness is rather limited. At $x/L_C = 1$, the δ_{995} thickness roughly corresponds to the left (i.e. near-wall) side of the vortex.

The formation of the secondary, positive-circulation vortex is a direct consequence of the cross-flow profile in the sidewall boundary layer. As can be observed in Fig. 9, the downward motion of low-momentum fluid generates a near-wall region of positive vorticity due to the no-slip condition at the wall. At a streamwise distance of $x/L_C = 0.78$, this vorticity sheet takes the form of a discrete
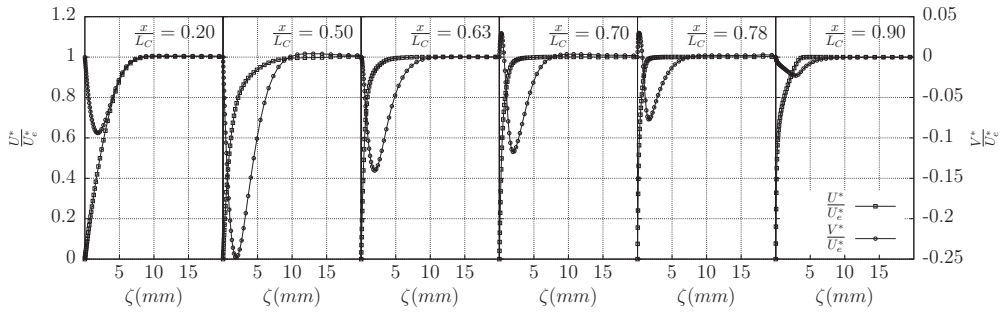
Figure 13. Streamwise and crossflow velocity profiles
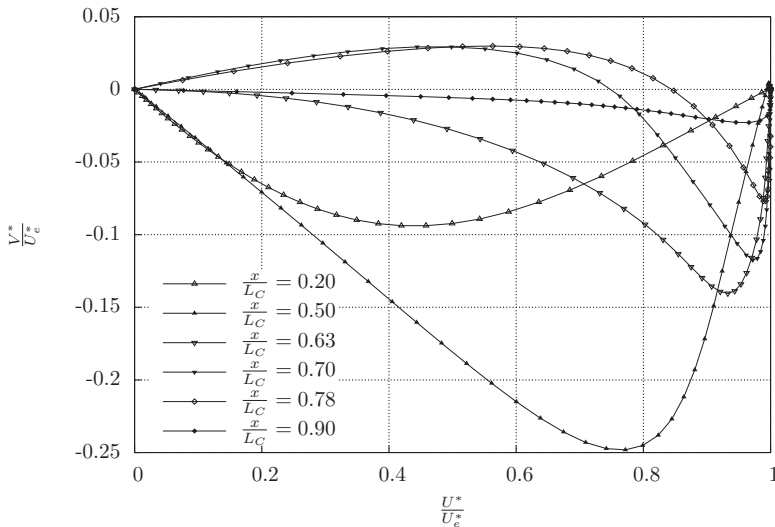on the streamline starting from $y/L_c = 0.182$ at different locations x/L_c.

Figure 14. Hodographic representation of the velocity profiles
on the streamline starting from $y/L_c = 0.182$ at different locations x/L_c.

vortex that deflects fluid particles towards the wall, thus producing the peak in c_f observed in Fig. 7 near the contraction centreline. In fact, the combination of positive and negative vorticity regions on both sides of the contraction creates a saddle point in the streamwise cut-planes at $y = 0$ and $z > 0$. At the contraction exit, this saddle point is located at about $z = 0.01$m away from the wall, which roughly corresponds to the thickness of the boundary layer. Therefore, the effect of the two pairs of streamwise vortices is not simply to thicken the boundary layer, as the classical explanation suggests[2,12,17], but to deform the boundary-layer profiles near the sidewall centreline (see also Fig. 6).

Finally, the small pocket of negative vorticity that can be observed near the wall for $x/L_C > 0.72$ has a different origin. In contrast with the two other vorticity regions, this feature only appears in the second half of the contraction. It is caused by a reversal of the lateral pressure gradient that is linked to the change of curvature of the potential-flow streamlines. This effect, which has not been reported so far, only influences the very near-wall region close to the sidewall centreline, owing to the small vertical momentum in this region.

To better illustrate the effect of lateral pressure gradients on the formation of streamwise vorticity, the velocity profiles normal to the sidewall were investigated within the framework of a streamline co-ordinate system[8,1]. The streamline co-ordinate system is a right-handed cartesian system, whose directions are defined by the directions of the tangent, the normal and the the binormal of a potential-flow streamline at a given point. Fig. 11 illustrates a typical three-dimensional boundary layer with crossflow, its associated streamline co-ordinate system (ξ,η,ζ) at an arbitrary point, as well as the original co-ordinate system (x,y,z). It should be noted that the origin of the local streamline co-ordinate system is located at the contraction sidewall, not at the streamline itself as shown in Fig. 11.

Velocity profiles were extracted at different streamwise locations for a streamline originating at $y/L_C = 0.182$ (the middle point of the contraction half-height at its inlet), and were transformed in the respective streamline co-ordinate system for each location. Fig. 12 shows the streamline as well as the local co-ordinate system (ξ,η,ζ) at an arbitrary point. Also shown in the figure is the position of the inflection point of the streamline $(x/L_C = 0.58)$.

Transformed streamwise (U^*) and crossflow (V^*) velocity profiles are presented in Fig. 13 for different x/L_C positions in the contraction. These profiles were normalised by the local streamwise velocity U^*_e in the potential flow. The U^* profiles have the shape of a typical two-dimensional boundary layer, with a decreasing thickness along the sidewall that is caused by the flow acceleration in the contraction. From the entrance of the contraction, a typical crossflow profile can also be observed. This crossflow profile is caused by the positive lateral pressure gradient $\partial p/\partial \eta > 0$ in the first half of the contraction (Fig. 12). The maximum magnitude of the crossflow pointing downwards is located at $x/L_c \approx 0.5$, slightly upstream of the streamline inflexion point. At this position, $\partial p/\partial \eta$ reaches its maximum. Further downstream, $\partial p/\partial \eta$ decreases and the magnitude of the downward motion decreases as well. Downstream of, $x/L_C = 0.63$ the V^* profile exhibits a portion, very near the wall, where the flow is moving upwards. This is caused by the negative sign of $\partial p/\partial \eta$ downstream of the inflection point. This upward deflection reaches a maximum at $x/L_C \cong 0.78$ and decreases afterwards. It is this upward deflection of near-wall fluid that is responsible for the creation the small pocket of negative vorticity observed near the wall in Figs 9 and 10.

A further practical representation of three-dimensional boundary-layer profiles is the hodographic diagram shown in Fig. 14, which represents the normalised crossflow velocity V^*/U^*_e as a function of the normalised streamwise velocity U^*/U^*_e. Upstream of the inflection point $(x/L_C = 0.58)$, the diagram has a classical 'triangular' shape that is representative of typical crossflow profiles as seen on an infinite swept wing[19,8,1,7]. Downstream of the inflection point, the diagram starts to deform until it becomes tangent to the the x-axis at its origin at $x/L_C = 0.63$. Then, further downstream, the diagram 'crosses over' to positive values of V^*/U^*_e near the wall. Finally, near the contraction exit, the crossflow profile slowly vanishes in the constant section part of the contraction. The behaviour observed in the hodographic diagram is fully consistent with the analysis performed on the profiles of Fig. 13.

5.0 DISCUSSION AND CONCLUSION

The numerical simulation of the flow inside the contraction of the TFT Boundary-Layer Wind Tunnel revealed a flow of considerable complexity. The observed secondary-flow patterns are generally consistent with the classical model of streamline confluence and skew-induced vorticity. However, viscous effects and the change of streamline curvature near the contraction exit tend to complicate the flow structure. In that respect, the analysis of boundary-layer profiles in the streamline co-ordinate system and the associated hodographic diagram proved very useful in interpreting the generation of secondary flows and streamwise vorticity near the contraction sidewalls.

The contours of boundary-layer thickness and the distribution of skin-friction coefficient extracted from the RANS simulation are consistent with measurements near the contraction exit. This gives confidence in the capability of the simulation to accurately reproduce the qualitative flow structure in the contraction. Nevertheless, it is important to highlight the potential weaknesses of the transition and turbulence models that were used. The laminar-turbulent transition was modeled as a simple 'switch' between a laminar and a turbulent zone, which necessarily simplifies the actual flow physics and neglects their possible spatial non-uniformity. Similarly, the SST $k - \omega$ turbulence model cannot be expected to fully reproduce the actual flow physics, mainly because of its reliance on the Boussinesq approximation, which is known to be relatively inaccurate for flows with significant curvature and vortical motions[32]. In order to obtain a better match between simulation and experiments, a more complex form of turbulence modelling, either in the form of a Reynolds-Stress-Transport Model or a Large-Eddy Simulation, along with more refined transition modelling, could be tested in the future. Nevertheless, the approach of flow modelling presented in this article proved very useful in understanding previously unknown aspects of the flow within the contraction.

The results presented above bring up the question of the influence of the contraction geometry on secondary-flow patterns and the effects of these secondary flows in a wind-tunnel test section. The fact that Mokhtari and Bradshaw[29] observed a reduction of c_f near the centreline at the exit of their 3:1 contraction, while there is a clear peak in c_f in the case of the 9:1 contraction of the TFT Boundary-Layer Wind Tunnel, suggests that the details of the flow structure depend on the actual contraction geometry. Furthermore, the state of the boundary layer on the contraction wall, and consequently the position of laminar-turbulent transition, probably have an effect as well. Indeed, in the preliminary results of Bouriga *et al*[6], simulations with a fully turbulent flow field revealed a flatter distribution of c_f at the contraction exit, although the general features of the secondary-flow patterns were similar to those presented here. This flatter distribution of c_f can be attributed to the stronger dissipation of vorticity by the turbulent boundary layer.

The potential effects of the longitudinal vortices on the flow in a test section mounted downstream of a constant-width contraction will mainly depend on the size of the test section and the purpose of the experiments carried out in the wind tunnel. As long as the sidewall boundary layers remain thin in comparison with the test section width, the influence of the vortices will be limited. Furthermore, the vortices are expected to slowly dissipate along the test-section wall, owing the the generally turbulent nature of the boundary layer[22]. Indeed, preliminary results of a CFD investigation of the flow in the test section of the TFT Boundary-Layer Wind Tunnel revealed that the influence of the vortices is limited downstream of the contraction[27]. Nevertheless, the deformed boundary-layer profiles observed by Bradshaw and Hellens in the NPL 50in × 9in. Boundary-Layer Wind Tunnel[9] are a reminder of the potentially long-lasting influence of secondary flows originating far upstream of a wind-tunnel test section.

ACKNOWLEDGEMENTS

REFERENCES

1. AHMED, F. and RAJARATNAM, N. Three-dimensional turbulent boundary layers: A review, *J Hydraulic Research*, **35**, (1), pp 81-98, 1997.
2. BANSOD, P. and BRADSHAW, P. The flow in S-shaped ducts, *Aeronaut Q*, 1972, **23**, pp 131-140.
3. BATCHELOR, G.K. *The theory of Homogeneous Turbulence*, Cambridge University Press, 1953.
4. BELL, J.H. and MEHTA, R.D. Boundary-layer predictions for small low-speed contractions, *AIAA J*, 1989, **27**, (3), pp 372-374.
5. BOURIGA, M. CFD investigation of Secondary Flow Effects in the Contraction of the TFT Boundary Layer Wind Tunnel, Master's thesis, University of Stuttgart, Germany, 2013.
6. BOURIGA, M., LEMYRE-BARON, J.-S., MORENCY, F. and WEISS, J. Preliminary experimental and numerical investigations of the flow in the contraction of a boundary-layer wind tunnel, *Transactions of the Canadian Society for Mechanical Engineering*, 2014, **38**, (4), pp 517-532.
7. BRADSHAW, P. and PONTIKOS, N.S. Measurements in the turbulent boundary layer on an 'infinite' swept wing, *J Fluid Mechanics,* 1985, **159**, pp 105-130.
8. BRADSHAW, P. Turbulent secondary flows, *Annual Review of Fluid Mechanics*, 1987, **19**, (1), pp 53-74.
9. BRADSHAW, P. and HELLENS, G.E. The N.P.L. 59 In. 9 In. Boundary-Layer Tunnel, Reports and Memoranda /Aeronautical Research Council. Her Majesty's Stationery Office, 1966.
10. BRADSHAW, P. and PANKHURST, R.C. The design of low-speed wind tunnels, *Progress in Aerospace Sciences*, 1964, **5**, pp 1-69.
11. CALAUTIT, J.K., CHAUDHRY, H.N., HUGHES, B.R. and SIM, L.F. A validated design methodology for a closed-loop subsonic wind tunnel, *J Wind Engineering and Industrial Aerodynamics*, 2014, **125**, pp 180-194.
12. CEBECI, T. and BRADSHAW, P. *Momentum Transfer In Boundary Layers*, McGraw-Hill, 1977.
13. CELIK, I.B., GHIA, U., ROACHE, P.J. and FREITAS, C.J. Procedure for estimation and reporting of uncertainty due to discretization in CFD applications, *J Fluids Eng – Transactions of the ASME*, 2008, **130**, (7).
14. COPLAND, J. ERCOFTAC Special Interest Group on Laminar to Turbulent Transition and Retransition: T3A and T3B Test Cases. 1990.
15. DRYDEN, H.L., SCHUBAUER, G.B., MOCK, W.C. and SKRAMSTAD, H.K. Measurements of intensity and scale of wind-tunnel turbulence and their relation to the critical Reynolds number of spheres. NACA Technical Report 581, 1937.
16. MENTER, F.R. Two-equation eddy-viscosity turbulence models for engineering applications, *AIAA J*, 1994, **32**, (8), pp 1598-1605.
17. GREITZER, E.M., TAN, C.S. and GRAF, M.B. *Internal Flow: Concepts and Applications*, Cambridge University Press, UK, 2004.
18. JASAK, H. *Error Analysis and Estimation for the Finite Volume Method with Applications to Fluid Flows*. PhD thesis, Department of Mechanical Engineering, Imperial College, London, UK, 1996.
19. JOHNSTON, JP. On the three-dimensional turbulent boundary layer generated by secondary flow, *J Basic Engineering*, 1960, **82**, (1), pp 233-246.
20. MEHTA, R.D. and BRADSHAW, P. Design rules for small low speed wind tunnels, *Aeronaut J*, 1979, **83**, (827), pp 443-449.
21. MEHTA, R.D. Turbulent boundary layer perturbed by a screen, *AIAA J*, 1985, **23**, (9), pp 1335-1342.
22. METHA, R.D. and BRADSHAW, P. Longitudinal vortices imbedded in turbulent boundary layers. Part 2: Vortex pair with 'common flow' upwards, *J Fluid Mechanics*, 1988, **188**, pp 529-546.
23. MOHAMMED-TAIFOUR, A., SCHWAAB, Q., PIOTON, J.and WEISS, J. A new wind tunnel for the study of pressure-induced separating and reattaching flows, *Aeronaut J*, 2015, **119**, (1211), pp 91-108.
24. MOONEN, P., BLOCKEN, B., ROELS, S. and CARMELIET, J.. Numerical modelling of the flow conditions in a closed-circuit low-speed wind tunnel, *J Wind Engineering and Industrial Aerodynamics*, 2006, **94**, (10), pp 699-723.
25. MOREL, T. Comprehensive Design of Axisymmetric Wind Tunnel Contractions, *J Fluids Eng*, 1975, **97**, (2), pp 225-233.
26. MOREL, T. Design of two-dimensional wind tunnel contractions, *J Fluids Eng*, 1977, **99**, (2), pp 371-377.
27. MUSLIN, B., BOURIGA, M., MORENCY, F. and WEISS, J. Numerical Investigations of the Flow inside a Wind-Tunnel Test Section. Proceedings of the 22nd Conference of the CFD Society of Canada, Toronto, Ontario, Canada, 2014.
28. PATANKAR, S.V and SPALDING, D.B. A calculation procedure for heat, mass and momentum transfer in three-dimensional parabolic flows, *Int J Heat and Mass Transfer*, 1972, **15**, (10), pp 1787-1806.

29 MOKHTARI, S. and BRADSHAW, P. Longitudinal vortices in wind tunnel wall boundary layers, *Aeronaut J*, 1983, **87**, pp 233-236.
30. TAVOULARIS, S. *Measurements in Fluid Mechanics*, Cambridge University Press, UK, 2005.
31. WELLER, H.G., TABOR, G., JASAK, H. and FUREBY, C. A tensorial approach to computational continuum mechanics using object-oriented techniques, *Computers in Physics*, 1998, **12**, (6), pp 620-631.
32. WILCOX, D.C. Turbulence modelling for CFD, DCW industries, La Cañada, Canada, 2006.